RSC Advances

ROYAL SOCIETY OF CHEMISTRY

PAPER

View Article Online
View Journal | View Issue

Check for updates

Cite this: *RSC Adv.*, 2022, **12**, 23786

Synthesis of manganese-oxide and palladium nanoparticles co-decorated polypyrrole/graphene oxide (MnO_2@Pd@PPy/GO) nanocomposites for anti-cancer treatment†

Jiarui Wu,‡[ab] Meng Wang,‡[a] Yuanjie Pan,[c] Yipeng Pang,[d] Yanyan Tang,[b] Chang Song,[c] Jiahui Zhu,[d] Xian Zhang[b] and Qingli Huang *[ac]

Received 23rd June 2022
Accepted 15th August 2022

DOI: 10.1039/d2ra03860a

rsc.li/rsc-advances

Design and fabrication of novel multifunctional nanomaterials as novel "theranostic nanoagents"with high efficiency and low side effects is important for cancer treatment. Herein, we synthesized manganese-oxide and palladium nanoparticle-co-decorated polypyrrole/graphene oxide (MnO_2@Pd@PPy/GO) nanocomposites, which could be used as a novel "theranostic nanoagent" for cancer treatment. Various spectroscopic and microscopic characterizations of the synthesized MnO_2@Pd@PPy/GO nanocomposites suggest that the nanocomposites are assembled sequentially by graphene oxide, polypyrrole, palladium nanoparticles and manganese-oxide nanoplates. Further research revealed that the nanocomposites had excellent photothermal conversion performance (reached near 50 °C after 10 min of irradiation), pH responsive enzymatic-like catalytic activity and enhanced magnetic resonance imaging (MRI) performance ($r_1 = 7.74$ mM^{-1} s^{-1} at pH 5.0 and glutathione (GSH)). Cell experiments also testified that combined cancer treatment (the viability of cancer cells is 30%) with photothermal therapy (PTT, the viability of cancer cells is 91% only with irradiation) and chemodynamic therapy (CDT, the viability of cancer cells is 74.7% only with nanocomposites) guided by MRI was achieved when the as-prepared nanocomposites were employed as theranostic nanoagents. This work could provide some new ideas for the controllable synthesis and application of multicomponent nanomaterials.

1. Introduction

Cancer is a high-mortality disease due to the lack of effective therapies because routine treatments (surgery, radiotherapy, and chemotherapy) have many side effects. Fortunately, advances in nanotechnology provide opportunities for the development of novel cancer diagnosis and therapies.[1–3] As an emerging therapy strategy based on nanotechnology, chemodynamic therapy (CDT), has received more and more attention due its many unique merits in increasing tumor specificity and decreasing side effects.[4–9] In CDT, cytotoxic ·OH was produced by employing the classical Fenton or Fenton-like reaction in the presence of metal-based nanomaterials (*e.g.*, Fe_3O_4, MnO_2 and Co_3O_4) in the tumor microenvironment (TME), where intracellular overexpressed hydrogen peroxide (H_2O_2), highly concentrated glutathione (GSH) and mild acidic condition existed. Then, the cytotoxic ·OH will induce severe oxidative damage to realize tumor treatment. Apart from CDT, photothermal therapy (PTT), as another emerging therapeutic modality based on nanotechnology, also has received increasing attention in recent years.[10–14] In PTT, site-specific nanomaterials with excellent photothermal conversion performance were employed in tumors. When the light irradiated on tumors, hyperthermia from nanomaterials will induce apoptosis and/or necrosis of cancer cells without damaging normal cells. Although many achievements were obtained in CDT and PTT, it is difficult to eradicate completely tumors depending on monotherapies. It is necessary to combinate cancer therapy of CDT with PTT or other therapeutic modalities due to superior anti-cancer activity than monotherapies.[15–21] Nanomaterials, particularly multifunctional nanocomposites, play a vital role in novel cancer therapies due to their good biodegradability, excellent catalytic activity, outstanding optical, magnetic performance, and unique synergistic effect.[22–26] They are incomparable to single-component nanomaterials because of their enhanced performances. However, comparing to single-component nanomaterials, the design and fabrication of multifunctional nanocomposites

---

[a] *Public Experimental Research Center, Xuzhou Medical University, Xuzhou City, Jiangsu 221004, China. E-mail: qlhuang@xzhmu.edu.cn; Fax: +86-516-83262091*

[b] *The First Clinical Medical College, Xuzhou Medical University, Xuzhou, Jiangsu 221004, China*

[c] *School of Pharmacy, Xuzhou Medical University, Xuzhou City, Jiangsu 221004, China*

[d] *School of Life Science, Xuzhou Medical University, Xuzhou City, Jiangsu 221004, China*

† Electronic supplementary information (ESI) available. See https://doi.org/10.1039/d2ra03860a

‡ These authors contributed equally to this work.

remains a significant challenge owing to different characteristics and complex forces of each component. How to effectively realize the orderly assembly of various components to achieve synergy is still an urgent problem to be solved.

Combining inorganic and organic nanomaterials is considered as an effective mean due to complementary performance and controllable interaction force.[27–32] Various binary or ternary inorganic–organic nanocomposites were prepared and used for cancer treatment.[33–36] However, quaternary inorganic–organic nanocomposites are less discussed, which may be due to their harder synthesis than binary or ternary inorganic–organic nanocomposites. Recently, graphene oxide (GO), polypyrrole (PPy), palladium (Pd) and manganese dioxide (MnO_2) based nanocomposites were widely used as drug carriers and cancer theranostic agents due to their fascinating properties.[37–40] Graphene oxide (GO), as one important graphene derivative, is an emerging extremely thin two-dimensional (2-D) nanomaterial in biomedicine due to its unique physicochemical properties.[41–43] Polypyrrole (PPy), a type of highly biocompatible conducting polymer also has been wide applications biomedical field thanks to their excellent physicochemical properties.[44–46] GO and PPy both can convert near infrared (NIR) light to heat and thus enable the NIR-responsive drug release for combined chemo-photothermal therapy owing to their aromatic and p-conjugated chemical bonds. However, they have few diagnostic applications in clinical treatment due to their poor optical and magnetic properties, which will limit the effective treatment of tumors. To solve these problems, by decorating some inorganic noble metal and metal oxide nanoparticles with diagnostic function on their surface could overcome these limitations and further expand the scope of diagnostic and therapeutic application. Pd, as one of noble metal, has plenty of superiorities including high thermal and chemical stability, tunable optical response, and catalytic effect, which has great potential in radioactive imaging and PTT.[47–49] Outstanding catalytic activity and CDT was found when Pd nanomaterials were used in tumor treatments.[47–49] Nanostructured manganese dioxide (MnO_2), a typical metal oxide, has attracted extensive attention in the field of anticancer applications owing to their strong oxidation ability, excellent catalytic activity, and good biodegradability.[50–56] MnO_2 can decrease the high GSH level and decompose H_2O_2 into H_2O and O_2 in tumor micro-environment (TME), which could regulate TME in tumor site. The released Mn^{2+} also can be used as magnetic resonance contrast agent. Amazing Fenton catalytic activity and magnetic resonance imaging (MRI) performance were arisen from the introduction of MnO_2. Making good use of these advantages will be an effective way to improve the curative effect of tumor.

On basis of the above discussions, a new nanocomposites manganese-oxide and palladium nanoparticles co-decorated polypyrrole/graphene oxide (MnO_2@Pd@PPy/GO) nanocomposite was synthesized. These four components are organically combined in harness other than messy mixed. Firstly, PPy was coated on the surface of GO by *in situ* polymeric reaction of pyrrole monomer to form PPy/GO. Then, Pd nanoparticles were formed on the surface of PPy/GO by reduction of $PdCl_2$ with $-NH_2$ of PPy. Finally, MnO_2 nanoplates were deposited on the surface of Pd@PPy/GO employing *in situ* redox reaction of $KMnO_4$ with PPy. Herein, PPy play a key role in the process of synthesis of MnO_2@Pd@PPy/GO nanocomposites. Excellent photothermal conversion performance, enzymatic-like catalytic activity and magnetic resonance imaging performance were obtained in following experiments. *In vitro* cells experiment, enhanced magnetic resonance imaging and synergistic therapeutic effects on MCF-7 cells were achieved. This work opens an opportunity to design novel cancer therapeutics, which would surely expand the biomedical application scope of nanocomposites.

2. Experimental section

2.1. Materials

All chemicals including pyrrole, ammonium persulphate ($(NH_4)_2S_2O_8$), hydrochloric acid (HCl), palladium chloride ($PdCl_2$), hydrogen peroxide (H_2O_2, 30% v/v), permanganate ($KMnO_4$), 3,3′,5,5′-tetramethylbenzidine (TMB) was purchased from the Sinopharm Chemical Reagent Co., Ltd (Shanghai, China) and used as received without further purification. Graphene oxide was purchased from XFNANO Co., Ltd (Nanjing, China). *In vitro* cell experiments, 2′,7′-dichlorofluorescin diacetate (DCFH-DA, 97%) propidium iodide (PI), calcein-AM, cell counting kit-8 (CCK-8), and fetal bovine serum were used.

2.2. Synthesis of MnO_2@Pd@PPy/GO nanocomposites

2.2.1. Construction of MnO_2@Pd@PPy/GO (GOPPMns). Firstly, PPy/GO (GOPs) was synthesized by adding 100 mg of pyrrole monomer into 35 mL graphene oxide (GO) dispersed solution (containing 10 mg GO) in presence of 340 mg of ammonium persulfate under the condition of ice bath and continued stirring for 30 minutes. The color of the solution changed from clear to black. And the PPy/GO (GOPs) was obtained by centrifugal separation to remove unreacted agents. Then, 200 μL of hydrochloric acid (1 M) and 2 mL $PdCl_2$ (0.1 M) solution were added into the prepared PPy/GO solution (containing 10 mg PPy/GO) and stirred overnight. After washing by centrifugation and redispersing in 20 mL of deionized water, the prepared Pd@PPy/GO (GOPPs, 20 mg) was added into $KMnO_4$ (40 mL, 0.1 M) aqueous solution and stirred for overnight. Finally, the prepared nanocomposites were collected by centrifugation, washed with distilled water and ethanol for several times, and finally dried in freeze dryer. 30 mg bovine serum albumin (BSA) was added into 10 mL GOPPMns (3 mg mL^{-1}) aqueous solution and stirred for overnight. Then, the precipitates were collected by the same procedure of GOPPMns.

2.3. Characterization of the as-prepared nanocomposites

Transmission electron microscopy (FEI, Tecnai 12, America), field-emission transmission electron microscopy (FEI, F-30, America) and scanning electron microscopy (FEI, Teneos VS, America) were employed to monitor the morphology of the as-prepared nanocomposites. All samples were doped on the sample SEM stage and dried in air. SEM images were acquired on SEM at 10 kV acceleration voltage. The UV-vis (AOE, UV-1902, China), FTIR (Thermo Fisher, NICOLET 5700, America) and

Raman spectra (Thermo Fisher, DXRxi, America) was used to characterize the information and structural change of the as-prepared nanocomposites, respectively. X-ray photoelectron spectra (XPS) were also obtained on an ESCALAB 250Xi system (Thermo Scientific, America) to further characterize the FePGMns. The surface potential of the as-prepared nanocomposites was obtained on a Zeta-sizer analyzer (Malvern, NICOMP 380ZLS, UK). In photothermal experiments, an 808 nm laser (Laserwave, 808 nm, China) and NIR camera (Fotric, S225, USA) was used. All MRI experiments were performed on a 3.0 T Discovery 750w MR system. Mn element concentrations were detected by inductively coupled plasma-optical emission spectrometer (Agilent, 725 ICP-OES, America).

2.4. Enzymatic-like catalytic activity of the as-prepared nanocomposites

TMB oxidation experiments were carried out by co-incubating TMB with the as-prepared nanocomposites. Various nanocomposites (30 μg) were added into 3 mL TMB buffer solution (containing TMB (1 mM) and H_2O_2 (0.1 mM)) at different pH values. The color change and UV-vis absorption at 652 nm were acquired. The generation capacity of O_2 of GOPPMns by catalyzing H_2O_2 was also discussed. The dissolved-O_2 concentration in solution was easily acquired on oxygen meter (JPBJ-608).

2.5. Photothermal conversion and enhanced MRI performance

To discuss the photothermal conversion performance of the as-prepared nanocomposites, an 808 nm near infrared (NIR, Beijing Laserwave OptoElectronics Technology Co., Ltd) laser and infrared thermal camera was employed. Typically, the as-prepared nanocomposites suspensions (1 mL) were placed in a plastic tube and irradiated with an 808 nm laser, which was monitored by an infrared thermal camera. Three consecutive laser-on/off cycles were also performed to evaluate the photothermal stability of GOPPs. The pH-responsive (pH 7.4, pH 7.4 + 10 mM GSH, and pH 5.0 + 10 mM GSH) enhanced MRI performance were investigated on a 3.0 T Discovery 750w MR

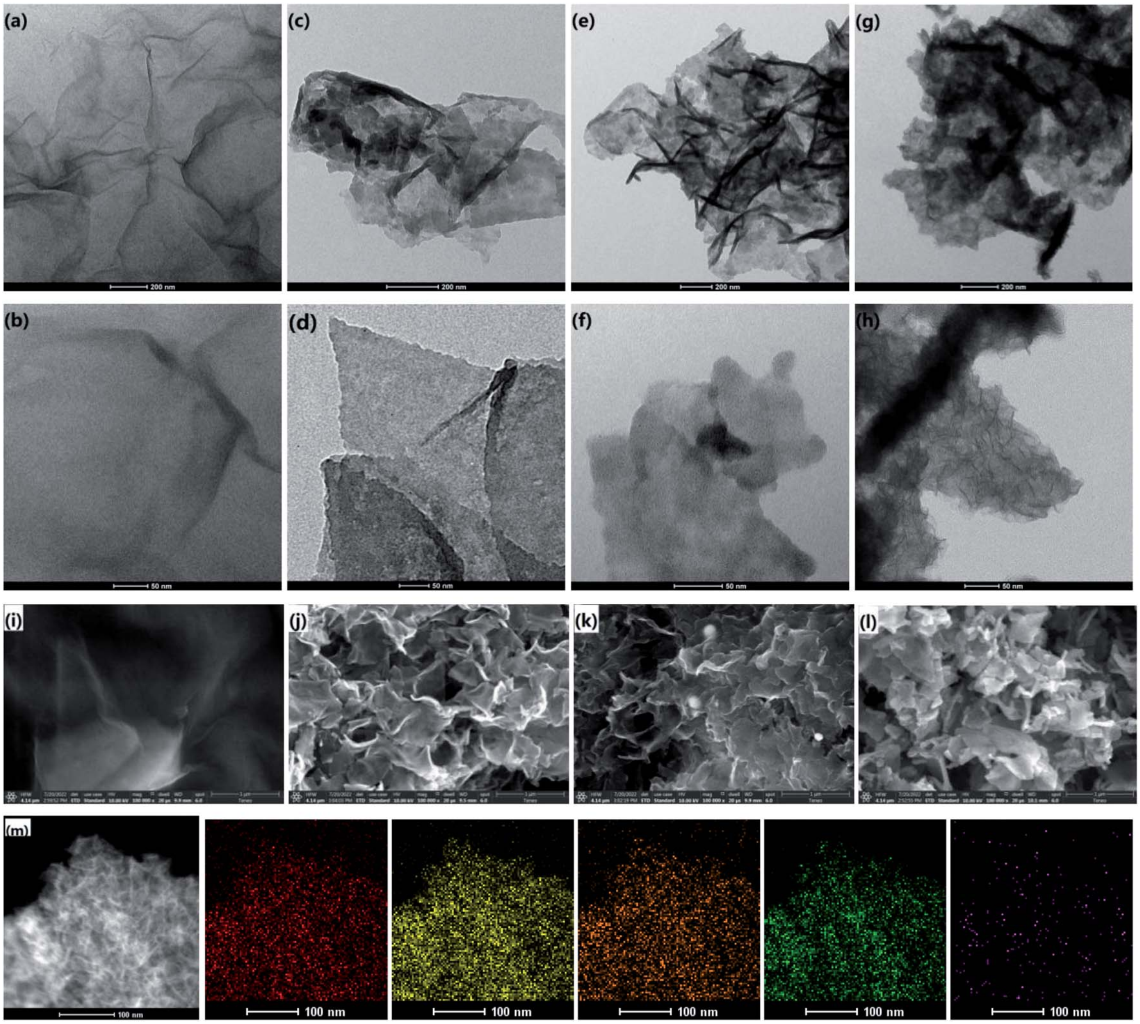

Fig. 1 TEM images of (a) and (b) GO (c) and (d) GOPs (e) and (f) GOPPs (g) and (h) GOPPMns, SEM images of (i) GO (j) GOPs (k) GOPPs (l) GOPPMns and (m) HAADF images and EDS mapping images of GOPPMns (carbon-red, nitrogen-yellow, oxygen-orange, manganese-green, and palladium-purple).

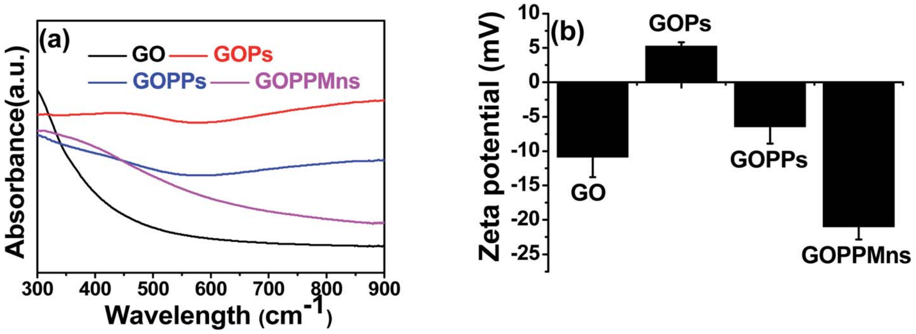

Fig. 2 (a) UV-vis (b) zeta potential of the as-prepared nanocomposites at pH 7.4.

system. MRI experiments of MCF-7 cells were also discussed after incubating GOPPMns (200 μg mL^{-1}, 37 °C) with cancer cells for 4 h.

2.6. The anti-cancer performance of GOPPMns

To evaluate the anti-cancer performance of GOPPMns. Mouse microglia BV2 cells and breast cancer MCF-7 cells were used to evaluate the biocompatibility and anti-cancer performance of GOPPMns and GOPPMns@BSA. Different concentrations of GOPPMns (GPPMns@BSA) were added and incubated with BV2 cells for 24 h, which was prepared in advance in 96-well plates. Then, the viability of cells was calculated based on standard CCK8 method. The anti-cancer performance of GPPMns@BSA was discussed by the same procedures except 808 nm NIR laser (1.5 W cm^{-2}, 5 min) irradiation was introduced before CCK8 method. To distinguish live and dead cells intuitively, calcein-AM and propidium iodide were used to co-stain the cells. Then, a fluorescence microscopy was used to observe the results. Intracellular hydroxyl radicals (HO·) in MCF-7 was investigated to discuss the CDT of GPPMns@BSA. DCFH-DA solution (1 mL, 10 μmol L^{-1}) was added into the preparative MCF-7 cells, which was incubated with the as-prepared nanocomposites in six-well plates for 4 h with or without 808 nm laser irradiation for 5 min. Finally, the fluorescence intensity in cells was observed by confocal laser scanning microscope (CLSM).

3. Results and discussion

3.1. Characterization of the nanocomposites

Transmission electron microscopy (TEM) and energy dispersive spectrometer (EDS) were used to characterize the as-prepared

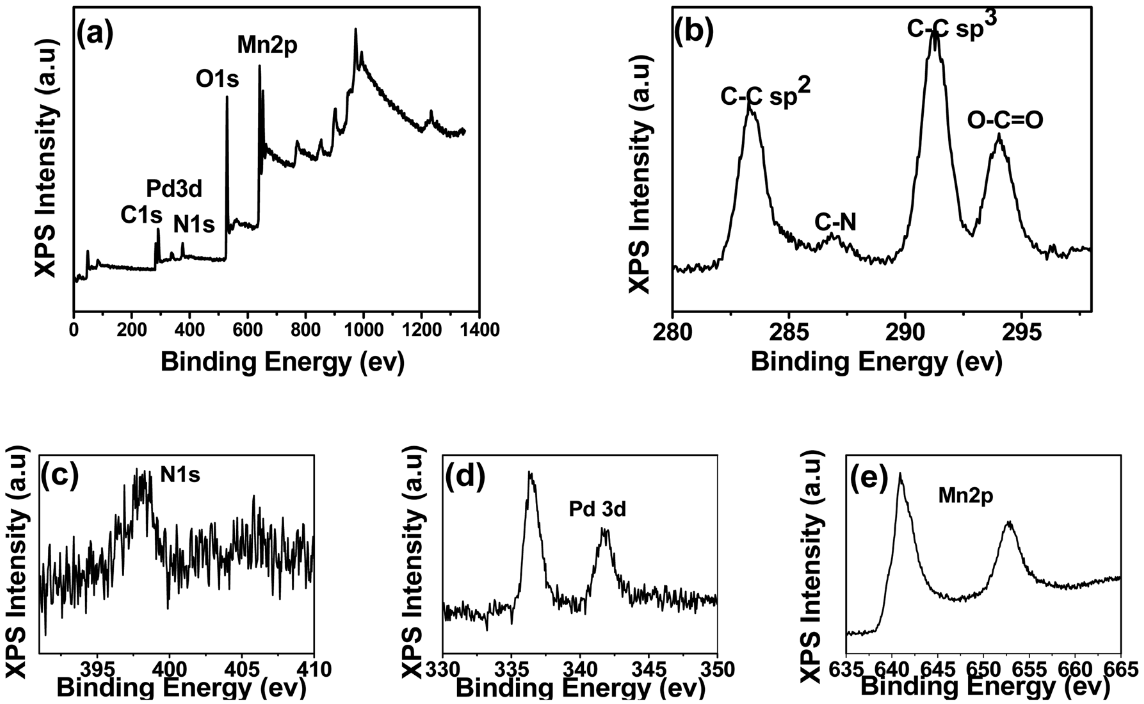

Fig. 3 X-ray photoelectron spectra (a) of GOPPMns and high-resolution X-ray photoelectron spectra of (b) C 1s, (c) N 1s, (d) O 1s, (e) Pd 3d and (f) Mn 2p.

nanocomposites. For GO, smooth surface was observed in Fig. 1a and b. For GO/PPy, the surface became rougher than that of GO when PPy was formed on GO in Fig. 1c and d. When $PdCl_2$ was introduced and reduced *in situ* by PPy, tiny nanoparticles (NPs) with diameter of 1–3 nm on the surface of GOPs were found in Fig. 1e and f, indicating the formation of Pd@PPy/GO (GOPPs). With following addition of $KMnO_4$, MnO_2 nanoplates were obtained on the surface of GOPPs in Fig. 1g and h, proving the preparation of MnO_2@Pd@PPy/GO (GOPPMns). SEM images of GO, GOPs, GOPPs and GOPPMns in Fig. 1i to l further confirmed this orderly way of assemble of GO, PPy, Pd and MnO_2, and the formation of MnO_2@Pd@PPy/GO. It is obvious that GOPPMns were constructed by assembling PPy, Pd NPs and MnO_2 nanoplates in succession on the surface of GO. Herein, PPy plays a key role because it can serve as reducing agent and linking molecule to reduce the Pd^{2+} and $KMnO_4$ *in situ* on the surface of GO. EDS spectrum of GOPPMns (Fig. S1†) and mapping (Fig. 1m) further confirmed the reliability of this result. C, N, O, Pd and Mn existed, which represented by colors in EDS mapping (carbon-red, nitrogen-orange, oxygen-yellow, manganese-green, and palladium-purple) in Fig. 1m. The high-resolution TEM (HRTEM) of the GOPPMns was also

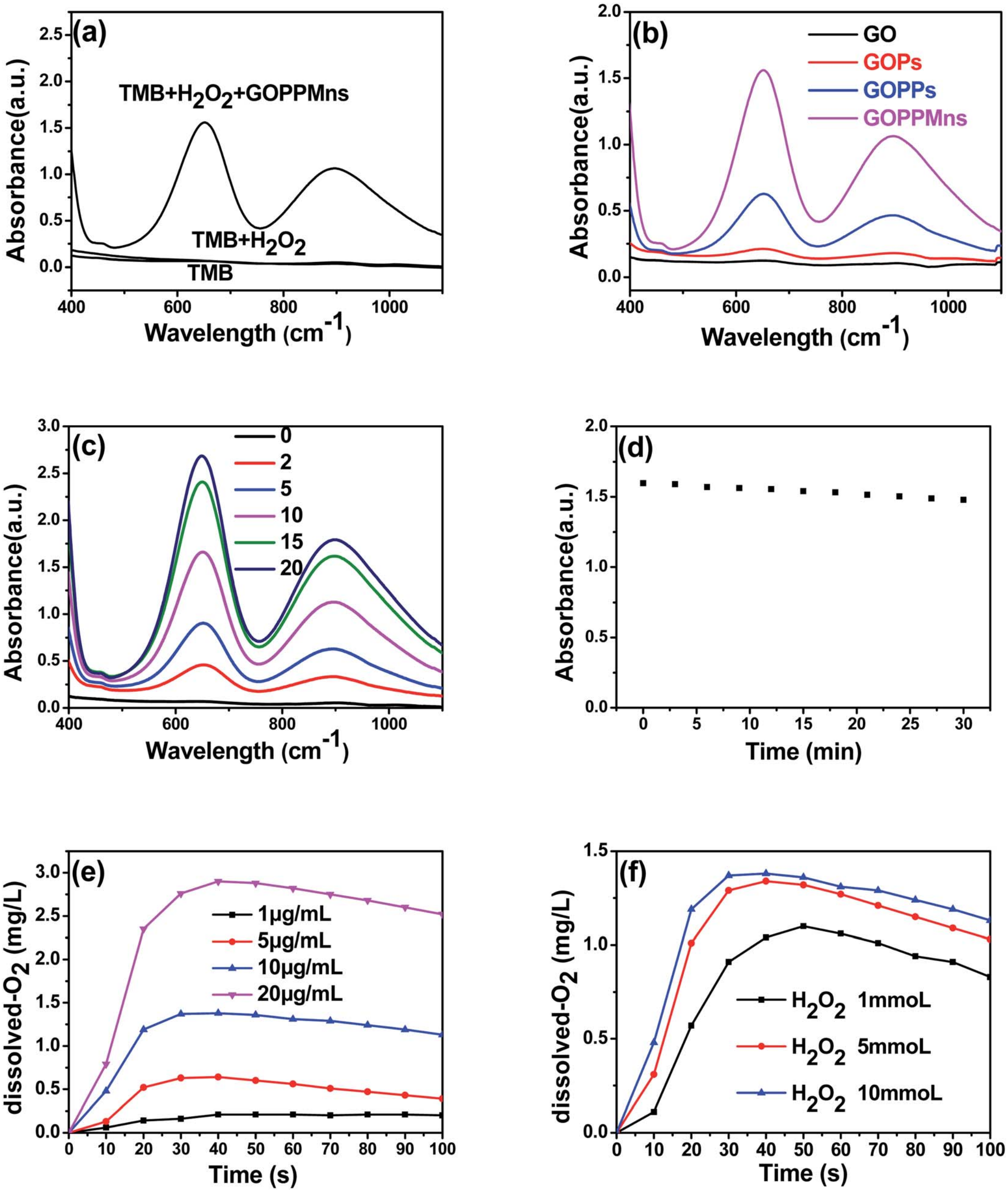

Fig. 4 Enzyme catalytic activity of GOPPMns on TMB at pH 5.0 (a) comparison of enzyme catalytic activity between GOPPMns and control (TMB and TMB + H_2O_2) (b) comparison of enzyme catalytic activity between GOPPMns and GO, GOPs, GOPPs. (c) Enzyme catalytic activity of GOPPMns with different concentration. (d) The stability of enzyme catalytic activity of GOPPMns. (e) O_2 generation ability of GOPPMns with different concentration (1 mmol L^{-1} H_2O_2 at pH 5.0). (f) O_2 generation ability of PPAuMns with different concentration of H_2O_2 (at pH 5.0, PPAuMns 10 μg mL^{-1}).

carried out to prove the assembling structure in Fig. S2a–e.† The lattice spacing of 0.34 nm and 0.23 nm corresponds to the (002) and (111) plane of GO and Pd, respectively (Fig. S2c and d†). However, no obvious lattice spacing was found due to poor crystallinity of MnO_2 (Fig. S2e†).

UV-vis spectroscopic method was used to further characterize the as-prepared nanocomposites. Obviously, strong absorbances at 600–900 nm in NIR region were found in GOPs and GOPPs, which will benefit photothermal conversion effect. For GOPPMns, the peak from 350 nm to 500 nm indicated the existence of MnO_2. Zeta potential also gave more details of the as-prepared GOPPMns. Great diversity on zeta potential of different nanocomposites in Fig. 2b testified the existence of Pd NPs and MnO_2 nanoplates, which are consistent with the results of TEM in Fig. 1.

The XPS technique was further applied to investigate the surface properties and compositions of GOPPMns. The survey spectrum of the GOPPMns shows that it was composed of elements C, N, O, Pd and Mn (Fig. 3a). And the high-resolution spectra of these elements were listed in Fig. 3b–f. In Fig. 3b, C–C sp^2 (283.4 eV), C–N (286.9 eV), C–C sp^3 (291.3 eV), and O–C=O (294.0 eV) bonds of graphitic carbon and pyrrole ring were observed for C 1s.[57,58] And in Fig. 3c, N 1s characteristics peaks were found in the range of 395 and 407 eV, which originated from pyrrolic N and graphitic N.[57,58] Obviously, GO and PPy are the organic component part in GOPPMns. For the inorganic component part, Pd $3d_{5/2}$ and Pd $3d_{3/2}$ are found at 336.4 eV and 341.8 eV in Fig. 3d; Mn ($2p_{1/2}$) and Mn ($2p_{3/2}$) were detected at around 652.8 and 640.9 eV in Fig. 3e. According to early reports, the palladium and manganese in the nanocomposite were in the valence of 0 and IV, respectively.[58,59] It was clear that the above data demonstrated that the as-prepared materials were manganese-oxide and noble metal palladium nanoparticles co-decorated polypyrrole/graphene oxide (MnO_2@Pd@PPy/GO) nanocomposites.

Noble metal palladium NPs and manganese-oxide nanoplates possessed excellent enzymatic-like catalytic activity, GOPPMns is expected to be very active enzymatic-like catalytic performance. To test this expectation, experiments were carried out by catalyzing TMB. There were no characteristic peaks of oxidized TMB from 400 nm to 1100 nm for TMB and TMB + H_2O_2 groups in Fig. 4a. For GOPPMns + TMB + H_2O_2 group, two obvious UV-vis absorption peaks at 652 and 895 nm in Fig. 4a were observed, indicating enzymatic-like catalytic activity of GOPPMns. Furthermore, the catalytic performance of GOPPMns was the highest in all groups (GO, GOPs, GOPPs and GOPPMns) in Fig. 4b and S3,† which indicated the significance of the presence of MnO_2. Meanwhile, the catalytic ability of GOPPMns were dependent on their concentrations and showed high stability in 30 min in Fig. 4c and d. According to the previous studies, the catalytic activity of nanocomposites is also related to the generation of O_2. The O_2 generation capacity of GOPPMns was furtherly studied at pH 5.0 using a dissolved-O_2 meter. It can be found that higher dissolved-O_2 concentrations were obtained with increase of GOPPMns and H_2O_2. All the conclusions suggested the as-prepared GOPPMns possessed excellent enzymatic-like catalytic activity and could be used as CDT for cancer. We also investigated the change on morphology

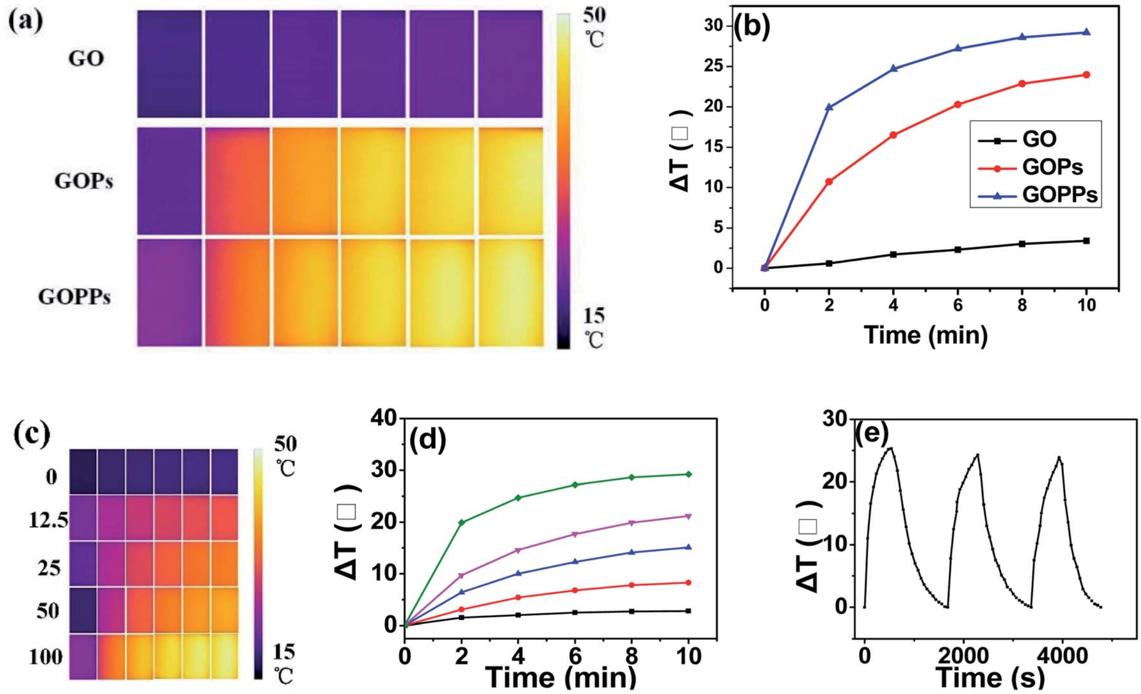

Fig. 5 (a) and (b) NIR laser (808 nm, 1.5 W, 10 min) irradiation-induced photothermal images and the corresponding temperature elevations of GO, GOPs and GOPPs with 100 μg mL^{-1}; (c) and (d) NIR laser (808 nm, 1.5 W, 10 min) irradiation-induced photothermal images and the corresponding temperature elevations of GOPPs with different concentration (0, 12.5, 25, 50 and 100 μg mL^{-1}). (e) Photothermal stability of GOPPs for three consecutive cycles.

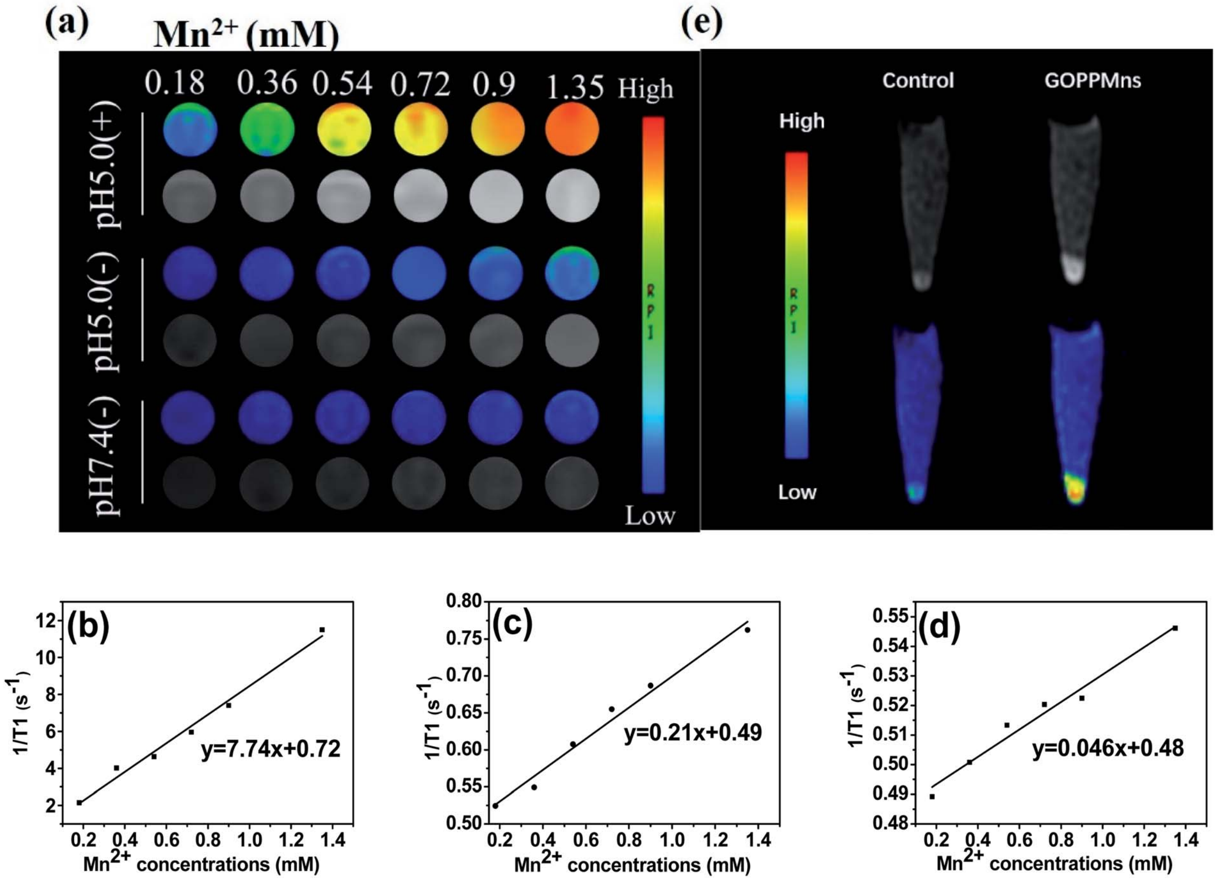

Fig. 6 (a) T1-weighted MR images of GOPPMns dispersions, and the transverse relativities (r_1) of GOPPMns dispersions in PBS at (b) pH 7.4 (c) pH 5.0 and (d) pH 5.0 + GSH, (e) T1-weighted MR images of MCF-7 cells incubated without and with GOPPMns.

of GOPPMns stored in 6 months by TEM and EDS mapping in Fig. S4.† There is little change, which can also prove stability and durability of the as-prepared nanocomposites.

The photothermal conversion capability of the as-prepared nanocomposites was evaluated (Fig. 5a and b). No obvious temperature variation in GO after irradiation (808 nm, 1.5 W, 10 min). However, the temperature of the GOPs and GOPPs solution (100 μg mL^{-1}) reached near 50 °C after 10 min of irradiation in Fig. 5a and b. Furthermore, the temperature of GOPPs solution increased significantly with increase of solution concentration in Fig. 5c and d. It is no doubt that excellent photothermal conversion capability was achieved by coupling PPy and decorating Pd NPs on GO sheets, which ensured irreversible damage to the cancer cells for photothermal therapy. The photothermal stability of GOPPs were also discussed. There is no continuous reduction in temperature variation after 3 heating and cooling cycles (Fig. 5e), indicating that its photostability was excellent.

MnO_2 is regarded as a potential T1 agent of MRI. The MRI experiments based on GOPPMns were carried out on a 3.0 T Discovery 750w MR system. As shown in Fig. 6a, enhanced pH-dependent and GSH dependent brightening effects were found in GOPPMns dispersions. At pH 7.4 without GSH, no visible MRI signal was observed in GOPPMns water dispersion. In contrast, an increasingly brighter trend with an increase in the Mn concentration was seen when the pH is 5.0 in the absence of GSH. When introducing GSH at pH 5.0, the brighter trend becomes more obvious as the Mn concentration increased. And the relaxivity of GOPPMns at various conditions was estimated to be 0.046, 0.21, and 7.74 mM^{-1} s^{-1} in Fig. 6b–d, respectively. Cells experiments also showed obvious MR enhancement signals in MCF-7 cells in Fig. 6e, manifesting the cellular uptake of GOPPMns by MCF-7 cells. These results further demonstrated that the as-prepared GOPPMns was TME (pH and GSH) responsive, which is an ideal agent as theranostic nanoagents for cancer.

For a cancer therapeutic agent, high safety and cytocompatibility *in vitro* are essential. Normal mouse microglia BV2 cells were chosen *in vitro* experiments. It can be found that some toxicity for normal cells was existed when 25 μg mL^{-1} GOPPMns was used and co-cultured with BV2 cells for 24 h in Fig. 7a. To amend the safety and cytocompatibility of GOPPMns, BSA, a biocompatible molecule, was used to modify the GOPPMns. The FTIR spectrum in Fig. 7b revealed that BSA was modified on the surface of GOPPMns. Surprisingly, there is almost no toxicity to normal BV2 cell when GOPPMns was replaced with GOPPMns@BSA in Fig. 7c. Obviously, GOPPMns@BSA is a more appropriate therapeutic agent rather

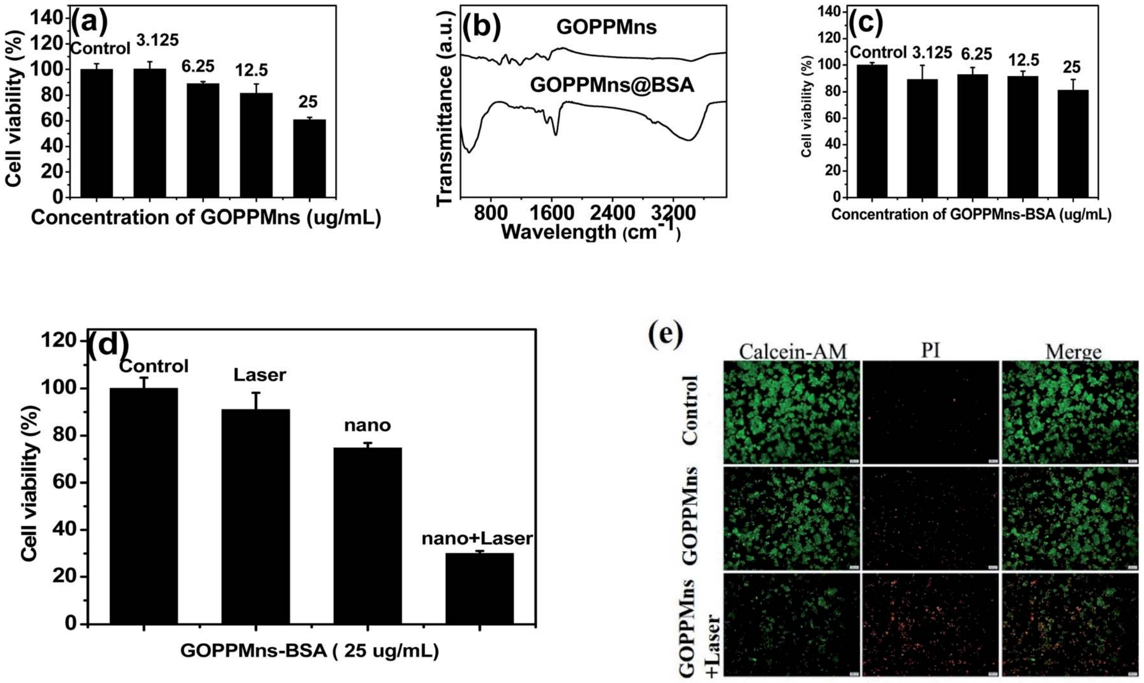

Fig. 7 (a) Viabilities of BV2 cells incubated for 24 h with different concentrations of GOPPMns (b) FTIR spectrum of GOPPMns and GOPPMns@BSA. (c) Viabilities of BV2 cells incubated for 24 h with different concentrations of GOPPMns@BSA (d) viability of MCF-7 cells incubated with 25 μg mL^{-1} GOPPMns@BSA for 24 h without and with NIR laser irradiation (e) live/dead assay of MCF-7 cells treated with PBS, GOPPMns@BSA and GOPPMns@BSA + laser. An 808 nm NIR laser was used at 1.5 W cm^{-2} for 5 min for the laser and GOPPMns@BSA + laser groups.

than GOPPMns for cancer. The anticancer performances of GOPPMns@BSA *in vitro* are discussed in Fig. 7d. It could be seen that there was almost no dead cell for control (only with PBS) and laser groups (without GOPPMns@BSA). However, when GOPPMns@BSA was added and co-incubated with MCF-7 cells for 24 h, the viability decreased to 74.7%, which may be due to the CDT effect was aroused in TME. Once laser irradiation and GOPPMns@BSA were employed simultaneously, the viability of MCF-7 was only 30%. This means that laser irradiation could activate the GOPPMns@BSA and PTT effect was achieved. To intuitively evaluate the anticancer performances of GOPPMns@BSA, calcein-AM and propidium iodide were used to distinguish live and dead cells on a fluorescence microscopy. Negligible death cell was seen in control group (only with PBS). And some died cells was observed when GOPPMns@BSA was adopted without any laser irradiation. Notably, most of cells died after treatment with GOPPMns@BSA under NIR irradiation. The results are consistent with the viability of cells in Fig. 7d. Obviously, the as-prepared GOPPMns had a lethal effect on the cancer cells *via* synergistic PTT and CDT.

The CDT efficiency of the nanocomposites depends seriously on the production of hydroxyl radicals (HO·). To prove the CDT

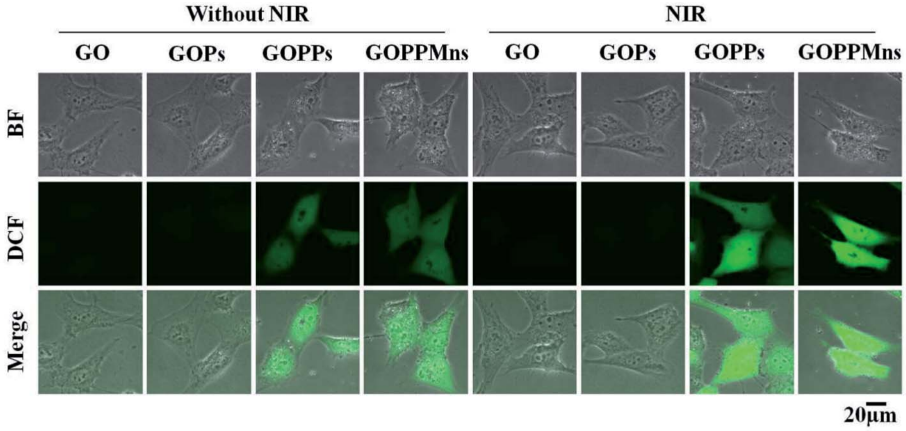

Fig. 8 Intracellular ROS images in MCF-7 cells after incubating GO, GOPs, GOPPs and GOPPMns without 808 nm laser irradiation and with 808 nm laser irradiation (scale bar = 20 μm).

Table 1 Similar particles in literature and their anti-cancer applications

NPs	NPs characteristics	Cancers	Anti-cancer methods	References
PPy	Nanospheres (60–90 nm)	Colon cancer HT29 cells	PTT and chemotherapy	12
GO-Pd	Pd (∼20 nm) unevenly distributed on GO	Prostate cancer PC3 cells	PDT and PTT	13
Pd@MnO_2	Pd distributed on MnO_2 nanosheets	Breast cancer MDA-MB-231	PTT and chemotherapy	34
Fe_3O_4@MnO_2@PPy	Sphere-like morphology (250 nm)	Liver cancer HepG2 cells	PDT, PTT and chemotherapy	60
MnO_2@Pd@PPy/GO	Pd and MnO_2 uniformly distributed on PPy/GO (50–200 nm)	Breast cancer MDA-MB-231	MRI, PTT, CDT potential for PDT and chemotherapy	This work

effect, intracellular ROS generation was evaluated using DCFH-DA as probe in Fig. 8. It could be seen that almost no green fluorescence signals were found when the cells were treated with GO and GOPs, respectively in Fig. 8a. Comparatively, obvious fluorescence signals were observed when the cells were incubated with GOPPs and GOPPMns, respectively. This phenomenon suggested that these intracellular ROS were produced primarily by Pd NPs and MnO_2 nanoplates on GOPPMns. Furthermore, enhanced fluorescence signals were observed under laser irradiation, which confirmed the synergistic effect between PTT and CDT in Fig. 8b. Obviously, comparing to other nanoagents reported in early literature in Table 1, both diagnosis and therapy were realized in the as-prepared nanocomposites, which is essential to improve the efficacy of cancer therapy.[12,13,34,60] That's for sure that the as-prepared GOPPMns are good candidate as "theranostic nanoagent" for synergistic PTT and CDT anti-cancer.

According to above results, the mechanism for the enhanced performance of the as-prepared MnO_2@Pd@PPy/GO was also discussed. On one hand, MnO_2@Pd@PPy/GO dissolve Mn(II) ions and Pd@PPy/GO under the mildly acidic conditions of the TME and activate the Fenton reaction and enzyme-like reaction. Excessive production of ·OH was produced, which can oxidize vital cellular constituents (DNA, proteins and lipids) and induce cell apoptosis or necrosis. And CDT for cancer cells was realized. On the other hand, the heat generated by photothermal effect using the released Pd@PPy/GO as photothermal agent could further destroy the cellular balance, which will also lead to cell apoptosis or necrosis. Thus, photothermal therapy (PTT) was achieved, furthermore, PTT will promote CDT according early reports, which will enhance the efficiency of anti-cancer.[34,61]

4. Conclusions

In summary, we successfully designed and synthesized a multi-component MnO_2@Pd@PPy/GO nanocomposites by *in situ* self-assembly technology of inorganic and organic nanomaterials. Comparing to unitary component nanomaterials, the as-prepared nanocomposites showed enhanced performance of anti-cancer due to their excellent photothermal conversion performance (reached near 50 °C after 10 min of irradiation), pH responsive enzymatic-like catalytic activity and enhanced magnetic resonance imaging (MRI) performance. Obviously, a novel nanoplatform of diagnosis and treatment for cancer was constructed using this nanocomposite as a "theranostic nanoagent". This present work would promote the construction and medical applications of multi-component and multi-functional nanocomposites.

Conflicts of interest

The authors declare that they have no known competing financial interests or personal relationships that could have appeared to influence the work reported in this paper.

Acknowledgements

This work was financially supported by Postdoctoral Research Funding Program of Jiangsu Province of China (1701133C).

References

1 S. G. Klochkov, M. E. Neganova, V. N. Nikolenko, K. Chen, S. G. Somasundaram, C. E. Kirkland and G. Aliev, *Semin. Cancer Biol.*, 2021, **69**, 190–199.
2 X. Suo, J. Zhang, Y. Zhang, X. J. Liang, J. Zhang and D. Liu, *J. Mater. Chem. B*, 2020, **8**, 3985–4001.
3 D. de Melo-Diogo, R. Lima-Sousa, C. G. Alves, E. C. Costa, R. O. Louro and I. J. Correia, *Colloids Surf., B*, 2018, **171**, 260–275.
4 S. L. Li, P. Jiang, F. L. Jiang and Y. Liu, *Adv. Funct. Mater.*, 2021, **31**, 2100243.
5 A. X. Li, X. X. Yang and J. Chen, *RSC Adv.*, 2021, **3**, 10540–10547.
6 Z. Tang, Y. Liu, M. He and W. Bu, *Angew. Chem., Int. Ed.*, 2019, **58**, 946–956.
7 Q. Chen, D. Yang, L. Yu, X. Jing and Y. Chen, *Mater. Horiz.*, 2020, **7**, 317–337.
8 J. Xin, C. Deng, O. Aras, M. Zhou, C. Wu and F. An, *J. Nanobiotechnol.*, 2021, **19**, 192.
9 H. Lin, Y. Chen and J. Shi, *Chem. Soc. Rev.*, 2018, **47**, 1938–1958.
10 S. He, J. Li, M. Chen, L. Deng and X. Wu, *Int. J. Nanomed.*, 2020, **15**, 8451–8463.

11 Y. Zhou, X. Jing and Y. Chen, *J. Mater. Chem. B*, 2017, **5**, 6451–6470.

12 B. Guo, J. Zhao, C. Wu, Y. Zheng, C. Ye, M. Huang and S. Wang, *Colloids Surf., B*, 2019, **177**, 346–355.

13 R. K. Thapa, Z. C. Soe, W. Ou, K. Poudel, J. H. Jeong, S. G. Jin, S. K. Ku, H. G. Choi, Y. M. Lee, C. S. Yong and J. O. Kim, *Colloids Surf., B*, 2018, **169**, 429–437.

14 Y. Song, Z. Qu, J. Li, L. Shi, W. Zhao, H. Wang, T. Sun, T. Jia and Y. Sun, *J. Alloys Compd.*, 2021, **881**, 160592.

15 B. Ma, Y. Nishina and A. Bianco, *Carbon*, 2021, **178**, 783–791.

16 B. Zhou, C. Yin, Q. Feng, Y. Wu, X. Pan, C. Liu, J. Tian, S. Geng, K. Wang, J. Xing, Y. Cao, P. Shou, Z. Yu and A. Wu, *Nanoscale*, 2021, **13**, 19085–19097.

17 T. He, C. Jiang, J. He, Y. Zhang, G. He, J. Wu, J. Lin, X. Zhou and P. Huang, *Adv. Mater.*, 2021, **33**, e2008540.

18 D. Fang, H. Jin, X. Huang, Y. Shi, Z. Liu and S. Ben, *Front. Chem.*, 2021, **9**, 789934.

19 Y. Dong, S. Dong, Z. Wang, L. Feng, Q. Sun, G. Chen, F. He, S. Liu, W. Li and P. Yang, *ACS Appl. Mater. Interfaces*, 2020, **12**, 52479–52491.

20 L. Zhang, Z. Yang, W. He, J. Ren and C. Y. Wong, *J. Colloid Interface Sci.*, 2021, **599**, 543–555.

21 J. Wang, J. Han, C. Zhu, N. Han, J. Xi, L. Fan and R. Guo, *Langmuir*, 2018, **34**, 14661–14669.

22 B. Li, X. Wang, S. Hong, Q. Wang, L. Li, O. Eltayeb, C. Dong and S. Shuang, *Food Funct.*, 2021, **12**, 6334–6347.

23 Y. He, J. Wan, Y. Yang, P. Yuan, C. Yang, Z. Wang and L. Zhang, *Adv. Healthcare Mater.*, 2019, **8**, e1801254.

24 T. E. Kim, H. J. Jang, S. W. Park, J. Wei, S. Cho, W. I. Park, B. R. Lee, C. D. Yang and Y. K. Jung, *ACS Appl. Bio Mater.*, 2021, **4**, 3453–3461.

25 Z. Cheng, M. Li, R. Dey and Y. Chen, *J. Hematol. Oncol.*, 2021, **14**, 85.

26 J. Ou, H. Tian, J. Wu, J. Gao, J. Jiang, K. Liu, S. Wang, F. Wang, F. Tong, Y. Ye, L. Liu, B. Chen, X. Ma, X. Chen, F. Peng and Y. Tu, *ACS Appl. Mater. Interfaces*, 2021, **13**, 38050–38060.

27 H. Follmann, A. F. Naves, R. A. Araujo, V. Dubovoy and O. N. Oliveira, *Curr. Pharm. Des.*, 2017, **23**, 3794.

28 J. Xing, Q. Gong, O. U. Akakuru, C. Liu, R. Zou and A. Wu, *Nanoscale*, 2020, **12**, 24311–24330.

29 M. Zhang, B. Li, Y. Du, G. Zhou, Y. Tang, Y. Shi, B. Zhang, Z. Xu and Q. Huang, *Chem. Eng. J.*, 2021, **424**, 130356.

30 S. Wang, Z. Zhou, G. Yu, N. Lu, Y. Liu, Y. Dai, X. Fu, J. Wang and X. Chen, *ACS Appl. Mater. Interfaces*, 2018, **10**, 28382–28389.

31 W. Feng, X. Zhou, W. Nie, L. Chen, K. Qiu, Y. Zhang and C. He, *ACS Appl. Mater. Interfaces*, 2015, **7**, 4354–4367.

32 A. Bg, B. Jz, A. Zz, A. Xiao, A. Mh and A. Sw, *Chem. Eng. J.*, 2019, **391**, 123609.

33 S. W. Jun, P. Manivasagan, J. Kwon, V. T. Nguyen, S. Mondal, C. D. Ly, J. Lee, Y. H. Kang, C. S. Kim and J. Oh, *Int. J. Biol. Macromol.*, 2020, **155**, 961–971.

34 C. Sun, Y. Liu, R. Zhou, L. Yao, R. Wang, W. Zang and W. Meng, *ACS Appl. Bio Mater.*, 2019, **2**, 4747–4755.

35 H. Wang, D. H. Bremner, K. Wu, X. Gong and L. M. Zhu, *Chem. Eng. J.*, 2019, **382**, 122848.

36 L. Han, Y. Zhang, Y. Zhang, Y. Shu, X. W. Chen and J. H. Wang, *Talanta*, 2017, **171**, 32–38.

37 R. Lima-Sousa, D. de Melo-Diogo, C. G. Alves, E. C. Costa, P. Ferreira, R. O. Louro and I. J. Correia, *Carbohydr. Polym.*, 2018, **200**, 93–99.

38 S. M. Mousavi, F. W. Low, S. A. Hashemi, N. A. Samsudin, M. Shakeri, Y. Yusoff, M. Rahsepar, C. W. Lai, A. Babapoor, S. Soroshnia, S. M. Goh, S. K. Tiong and N. Amin, *RSC Adv.*, 2020, **10**, 12851.

39 D. de Melo-Diogo, R. Lima-Sousa, C. G. Alves and I. J. Correia, *Biomaterials*, 2019, **7**, 3534–3551.

40 N. Ahmad, S. Sultana, S. M. Faisal, A. Ahmed, S. Sabir and M. Z. Khan, *RSC Adv.*, 2019, **9**, 41135.

41 J. Liu, J. Dong, T. Zhang and Q. Peng, *J. Controlled Release*, 2018, **286**, 64–73.

42 S. Song, H. Shen, Y. Wang, X. Chu, J. Xie, N. Zhou and J. Shen, *Colloids Surf., B*, 2020, **185**, 110596.

43 Z. Gu, S. Zhu, L. Yan, F. Zhao and Y. Zhao, *Adv. Mater.*, 2019, **31**, e1800662.

44 X. Shan, Q. Chen, X. Yin, C. Jiang, T. Li, S. Wei, X. Zhang, G. Sun, J. Liu and L. Lu, *J. Mater. Chem. B*, 2020, **8**, 426–437.

45 S. Han and Y. Kim, *Colloids Surf., A*, 2019, **570**, 414–419.

46 Y. Yin, Y. Hao, N. Wang, P. Yang, N. Li, X. Zhang, Y. Song, X. Feng and W. Ma, *RSC Adv.*, 2020, **10**, 7771–7779.

47 Y. Liu, J. Li, M. Chen, X. Chen and N. Zheng, *Theranostics*, 2020, **10**, 10057–10074.

48 J. W. Xiao, S. X. Fan, F. Wang, L. D. Sun, X. Y. Zheng and C. H. Yan, *Nanoscale*, 2014, **6**, 4345–4351.

49 A. Dumas and P. Couvreur, *Chem. Sci.*, 2015, **6**, 2153–2157.

50 L. S. Lin, J. Song, L. Song, K. Ke, Y. Liu, Z. Zhou, Z. Shen, J. Li, Z. Yang, W. Tang, G. Niu, H. H. Yang and X. Chen, *Angew. Chem., Int. Ed. Engl.*, 2018, **57**, 4902–4906.

51 D. Gu, Z. Liu, H. Wu, P. An, X. Zhi, Y. Yin, W. Liu and B. Sun, *Colloids Surf., B*, 2021, **199**, 111538.

52 J. Wen, K. Yang and S. Sun, *Chem. Commun.*, 2020, **56**, 7065–7079.

53 J. Zhang, D. Bian, G. Shao, H. Wang and C. Wang, *J. Alloys Compd.*, 2021, **870**, 159415.

54 M. H. Cho, E. S. Choi, S. Kim, S. H. Goh and Y. Choi, *Front. Chem.*, 2017, **5**, 109.

55 Y. Wang, Y. Song, G. Zhu, D. Zhang and X. Liu, *Chin. Chem. Lett.*, 2018, **29**, 1685–1688.

56 X. Cai, Q. Zhu, Y. Zeng, Q. Zeng and Y. Zhan, *Int. J. Nanomed.*, 2019, **14**, 8321–8344.

57 S. Ramesh, H. M. Yadav, K. Karuppasamy, D. Vikraman and H. S. Kim, *J. Mater. Res. Technol.*, 2019, **8**, 4227–4238.

58 T. Liu, Z. Cui, Y. Liu and X. Bai, *Appl. Catal., A*, 2019, **588**, 117278.

59 D. Hou, H. Tao, X. Zhu and M. Li, *Appl. Surf. Sci.*, 2017, **419**, 580–585.

60 C. Qi, W. Wang, P. Wang, H. Cheng, X. Wang, B. Gong, A. Xie and Y. Shen, *Molecules*, 2022, **7**, 27.

61 M. Wang, G. Zhou, Y. Pan, Y. Xue, S. Zhu, Y. Yan, H. Yuan, S. Li and Q. Huang, *Mater. Des.*, 2022, **219**, 110794.